

# Multimodal, Nanoscale, Hyperspectral Imaging Demonstrated on Heterostructures of Quantum Dots and DNA-Wrapped Single-Wall Carbon Nanotubes

Hyeonggon Kang,<sup>†</sup> Matthew L. Clarke,<sup>†</sup> Jianyong Tang,<sup>†</sup> John T. Woodward,<sup>†</sup> Shin G. Chou,<sup>†</sup> Zhenping Zhou,<sup>‡</sup> Jeffrey R. Simpson,<sup>‡,§</sup> Angela R. Hight Walker,<sup>†</sup> Tinh Nguyen,<sup>‡</sup> and Jeseong Hwang<sup>†,\*</sup>

<sup>†</sup>Optical Technology Division, Physics Laboratory, and <sup>‡</sup>Materials Research and Construction Division, NIST, Gaithersburg, Maryland 20899. <sup>§</sup>Current address: Department of Physics, Astronomy, and Geosciences, Towson University, Towson, Maryland 21204

In the past few years, advances in the controlled assembly of nanoscale building blocks (NBBs) have resulted in functional devices such as nano-optoelectronic components, biophotonic nanosensors, and novel contrast probes for molecular imaging.<sup>1–7</sup> The NBBs employed for these applications include organic molecules (*e.g.*, polymers, nucleic acids, and proteins), metallic nanoparticles (*e.g.*, gold or silver nanoscale spheres, rods, and shells), semiconductor nanocrystals (quantum dots, QDs), and single-wall carbon nanotubes (SWCNTs).<sup>8</sup> In the assembled structures, final structural stability and functionality are primarily dependent upon the physicochemical properties of individual NBBs; however, the interactions of the NBBs in the assembly also play an important role.<sup>9,10</sup> Accordingly, physicochemical characterization of their interactions is key to predicting the function of the assembled complexes.

Recent efforts to engineer optoelectronic devices using novel hetero-NBB assemblies have employed a variety of techniques to optimize the optical and electrical properties of the final product.<sup>10,11</sup> In these systems, controlled transfer between electrical and photonic energy is critical for the development of functional optoelectronic devices. Among other heterostructure hybrids, conjugates of QDs and SWCNTs have increasingly been used for a variety of optoelectronic applications in an effort to engineer functional optoelectronic components and devices.<sup>12–20</sup> The size-dependent tunable band gaps of QDs and SWCNTs have

**ABSTRACT** A multimodality imaging technique integrating atomic force, polarized Raman, and fluorescence lifetime microscopies, together with 2D autocorrelation image analysis is applied to the study of a mesoscopic heterostructure of nanoscale materials. This approach enables simultaneous measurement of fluorescence emission and Raman shifts from a quantum dot (QD)—single-wall carbon nanotube (SWCNT) complex. Nanoscale physical and optoelectronic characteristics are observed including local QD concentrations, orientation-dependent polarization anisotropy of the SWCNT Raman intensities, and charge transfer from photoexcited QDs to covalently conjugated SWCNTs. Our measurement approach bridges the properties observed in bulk and single nanotube studies. This methodology provides fundamental understanding of the charge and energy transfer between nanoscale materials in an assembly.

**KEYWORDS:** carbon nanotube · quantum dot · energy transfer · nanoassembly · hyperspectral imaging

enabled fabrication of hybrid structures with desirable properties such as controlled photoinduced charge transfer from one species to the other.<sup>18,21</sup> Raman spectroscopy has been successfully employed to examine the structural and charge transfer characteristics of SWCNTs. However, the signal can be obscured in SWCNT structures conjugated to fluorescent materials, whose intensity can be orders of magnitude larger.

Monitoring the local orientation of SWCNTs in the heterostructure is of interest to quantitatively interrelate the structural parameters and physical properties of an assembly with heterogeneous composition. In a study to control the optical responses of SWCNTs and their interactions with other species in a heterostructure, polarized Raman spectroscopy was demonstrated as a useful measure of SWCNT orientation.<sup>22</sup> In the heterostructure of fluorescent QDs and SWCNTs, simultaneous

\*Address correspondence to jch@nist.gov.

Received for review August 24, 2009 and accepted October 14, 2009.

Published online October 21, 2009. 10.1021/nn901075j

This article not subject to U.S. Copyright. Published 2009 by the American Chemical Society.

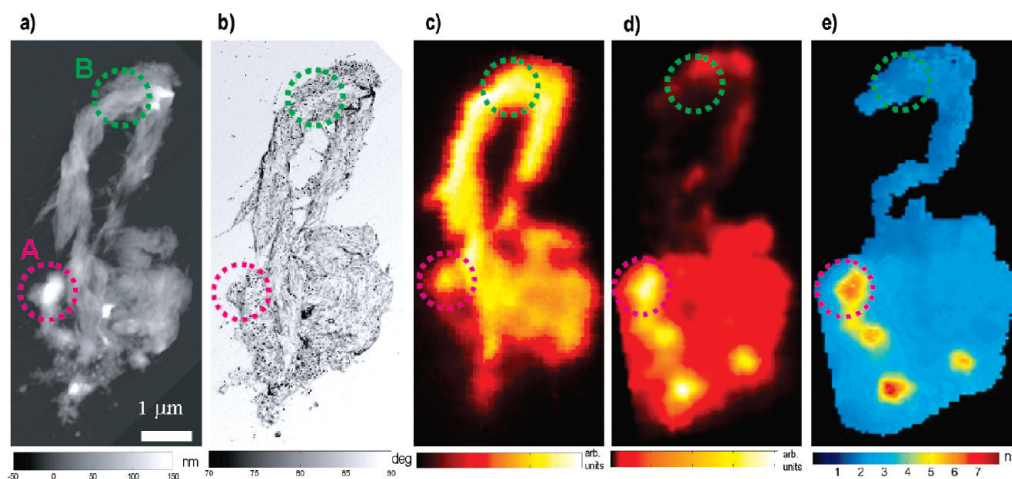


**Figure 1.** Multimodal imaging of SWCNT–QD complex. (a) AFM topography, (b) AFM phase image, (c) confocal micro-Raman image of the total integrated G band intensity ( $1500\text{--}1660\text{ cm}^{-1}$ ) of SWCNTs excited at 488 nm and combining two polarizations obtained from the hyperspectral map, (d) confocal fluorescence image of QDs excited at 488 nm and collected in the spectral region of  $\lambda > 585\text{ nm}$  obtained from the hyperspectral map, and (e) fluorescence lifetime map of QDs. Colored dashed circles are shown as reference points in the discussion.

hyperspectral imaging of fluorescence and Raman signatures would be extremely useful. Together, dynamic fluorescence emission signatures, such as photoluminescence lifetime and emission spectra of QDs, and Raman spectra of interacting SWCNTs provide better understanding of the photoinduced excitonic charge transfer from QDs to SWCNTs.

Therefore, in this study, we present a multimodal optical imaging platform, integrating confocal microscopy of simultaneous polarized Raman and fluorescence emission, fluorescence lifetime, atomic force microscopy, and its 2D autocorrelation analysis. This integrated approach allows us to study optical characteristics of the heterostructure in depth and to interrelate the optical properties with the detailed structure of its nanoscale constituents. Our time-dependent spectroscopic imaging results demonstrate dynamic, noninvasive measurements of photoinduced charge transfer among NBBs that allow a better understanding of the energy transfer mechanism in QD–SWCNT heterostructures. A QD–SWCNT heterostructure was chosen to demonstrate our unique metrology platform. The synthesis to combine QDs with DNA-wrapped SWCNTs is detailed elsewhere and summarized in the Methods section.<sup>23</sup> The lifetime imaging capability also provides spatially resolved information about the interactions between different species in a heterogeneously distributed sample. Such detailed information on localized intermolecular interactions in a bulk sample cannot be obtained by topological characterization or other imaging techniques.

## RESULTS AND DISCUSSION

A specific QD–SWCNT complex with a distinctive structure that contained several regions with different morphologies was selected to be the focus of the illustration of our multimodal imaging technique (Figure 1).

Atomic force microscopy (AFM) and optical microscopy reveal an  $8\text{ }\mu\text{m}$  long by  $4\text{ }\mu\text{m}$  wide structure containing a loop component on the top portion. AFM topography displays several round features along the bottom (*e.g.*, see circle A) and the very top of the heterostructure, while the remaining structure is dominated by elongated features (*e.g.*, circle B). We assign these morphologies as QD aggregates and SWCNT bundles, respectively. Additionally, in the AFM phase image (Figure 1b), small filaments are observed protruding from the main structure. AFM topography images show these filaments are  $1.5\text{--}4.0\text{ nm}$  high and thus consist of single or small bundles of nanotubes (see Supporting Information). This size can be contrasted with the larger bundles in the main structure which are  $20\text{--}100\text{ nm}$  in diameter. The AFM phase image reveals the decoration of QDs along the SWCNT bundles. The QDs appear as dark spots in the phase image.

Although the overall boundary and shape of the QD fluorescence emission (Figure 1d) concurs well with the AFM topographic pattern, local intensity correlation is not consistent, implying non-uniform conjugation of QDs to SWCNTs. Recent studies demonstrated SWCNT quenching of QD fluorescence when conjugated within nanoscale proximity.<sup>24</sup> Therefore, changes in the SWCNT density in the complex presented here could affect the QD fluorescence signal distribution. Specifically, the spatial SWCNT concentration should anticorrelate with the QD fluorescence if SWCNT-induced quenching is the primary factor for QD fluorescence quenching. To test this hypothesis, we performed Raman spectroscopic imaging to evaluate the spatial distribution of SWCNTs. Figure 1c shows a confocal micro-Raman image of the integrated G band intensity ( $1500\text{--}1660\text{ cm}^{-1}$ ) of SWCNTs within the complex. These data are the combination of two orthogonal ex-

citation polarizations. A nearly constant Raman intensity over the entire sample area indicates that the SWCNT distribution is uniform and suggests that the heterogeneous distribution of QDs is the primary cause for the modulated fluorescence pattern. This is consistent with our AFM image, which exhibits a relatively uniform distribution of the bundled fiber-like SWCNTs but non-uniform QD distribution, with clusters observed in the regions showing strong QD fluorescence signal. Therefore, we conclude that SWCNT quenching is not responsible for the QD intensity distribution.

Our primary interest in this report is to interrelate optical microscopy with the nanoscale structure of the complex. The nanoscale topographical information is well-demonstrated in our AFM image (Figure 1a,b). The bundled SWCNT structures appear to have a highly ordered local orientation, and we would predict significant Raman polarization behavior. The AFM phase image (Figure 1b) highlights the orientation of SWCNT bundles and enables visualization of the nanoscale texture of the QD–SWCNT complex. As a quantitative measure of this local orientation, spatial 2D autocorrelation analysis was performed on the AFM phase image.<sup>25</sup> In brief, we are examining the mean orientation of the image texture, and we extract information about the SWCNT orientation angle distribution. Figure 2a shows the AFM phase image and its 2D autocorrelation results (overlaid red lines). The red lines show the local orientation angle as well as the orientation strength (shown by the line length).

Polarization-dependent Raman spectroscopy of SWCNTs has been previously demonstrated.<sup>26–29</sup> Due to the strong anisotropy of the SWCNT optical response, the Raman intensity varies as a function of the angle between the nanotube axis and the incident light polarization. This functional dependence when combined with the autocorrelation results (based on AFM phase images) predicts the Raman polarization images shown in Figure 2b,c. This calculation identifies regions of the complex that are expected to exhibit polarization-dependent Raman signal. For example, the large section on the left side of Figure 2b suggests that strong Raman signals would be observed in this region when excited by light polarized parallel to the complex long axis. Conversely, when the sample is rotated 90°, this area should exhibit much weaker Raman signal, while the signal from the top section in Figure 2c would be increased. Indeed, when compared to the experimen-

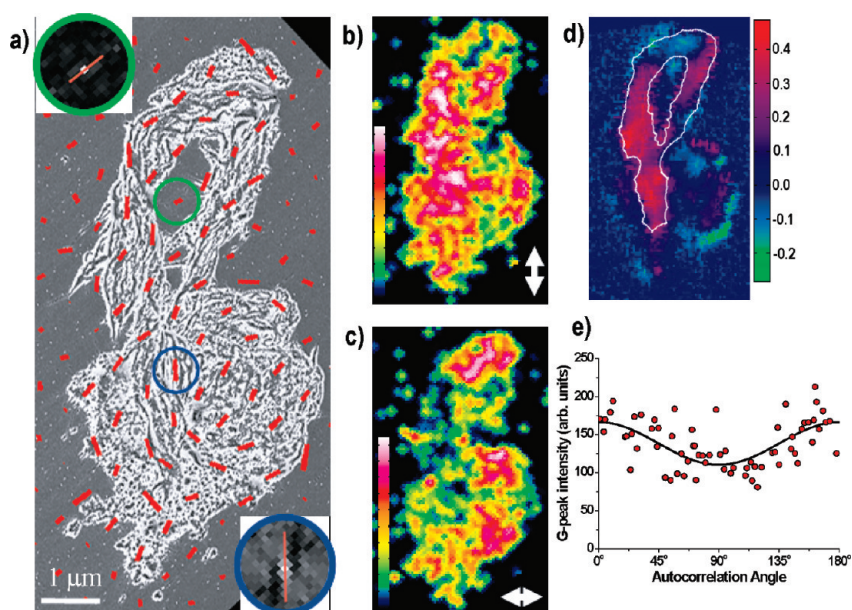


**Figure 2.** AFM phase image with its 2D autocorrelation pattern with predicted and experimental polarized Raman signals. (a) AFM phase image with 2D autocorrelation results for  $16 \times 16$  pixel regions shown in red. For clarity, only every other autocorrelation line is displayed. The angles of the red lines indicate the maximum correlation angle, and the length of the line represents the correlation strength at that angle. Inset: the log of the autocorrelation images from two highlighted regions is shown with lines indicating the angle of maximum correlation. (b,c) Polarized Raman G peak intensities for the incident polarization indicated by arrows predicted using all autocorrelation results. (d) Experimentally measured Raman G peak polarization anisotropy. Red areas indicate larger Raman intensity when excited by a laser polarized parallel to the heterocomplex long axis. Green areas are more intense when excited by perpendicular light. (e) Experimental Raman G peak intensity as a function of the autocorrelation angle for regions outlined in white in (d) with a fit to  $\cos^2 \theta$ . To account for the two polarizations, the autocorrelation angles were offset by  $90^\circ$  for the second polarization.

tally measured G peak anisotropy image (Figure 2d) selected from a series of confocal polarization-dependent hyperspectral images (details of which are discussed below), the calculated image pattern relates well with the observed local Raman polarization dependence.

Selected image slices for the measured G and G' Raman peaks of SWCNTs and fluorescence signal of QDs from the full hyperspectral image data set (see Supporting Information) are shown in Figure 3b,c. A reference spectrum from one image pixel is shown in Figure 3a. It is noted that the polarization dependence of the experimental G and G' peaks corresponds well with the Raman dependence estimated by the autocorrelation image (Figure 2b,c). Strong enhancement of the Raman signal can be observed when the polarization is parallel to the bundled SWCNT orientation. The experimental G peak intensities for each polarization angle match the predicted Raman polarization signals very well. To further compare the autocorrelation results with the experimental, polarization-dependent Raman G peak signal, the measured local Raman intensity in highly orientated regions is plotted as a function of the autocorrelation angle (Figure 2e). The G peak Raman intensity *versus* orientation angle of SWCNT alignment fits to a  $\cos^2 \theta$  dependence though the scatter in the data is large. These outlying data points are indicators

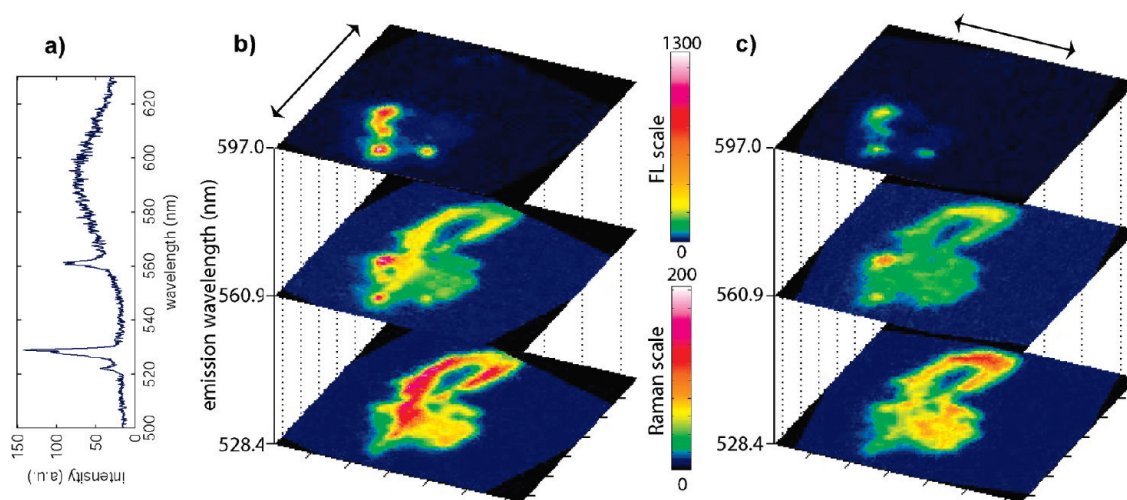


**Figure 3.** Intensity images plotted from Raman and fluorescence peaks. (a) Example spectrum from one pixel with Raman and fluorescence peaks. (b,c) Wavelength slice images showing the two major Raman peaks: G band, 528.4 nm ( $1567\text{ cm}^{-1}$ ); G' band, 560.5 nm ( $2651\text{ cm}^{-1}$ ), and the QD fluorescence (597 nm) excited using 488 nm light, linearly polarized in the directions indicated by the arrows.

of both limited spatial resolution of confocal Raman detection and limitations of the 2D spatial autocorrelation analysis. Additionally, when comparing the entire Raman and autocorrelation estimation images, it is observed that the autocorrelation results exaggerate the magnitude of the polarization effects. This is due to some assumptions made when performing the estimation. The autocorrelation data are based on the AFM phase results, which are probing the SWCNT–air interface. Variation in the SWCNT alignment beneath this surface layer is possible. When calculating the polarization effects from the autocorrelation results, we assume that each region has a single orientation angle, whereas in reality there will be a distribution of angles from the many SWCNTs present in the bundle.

A recent report demonstrated that the average fluorescence lifetime from QDs is significantly reduced after conjugation with SWCNTs, and this is attributed to either resonance energy transfer or an increased rate of nonradiative relaxation due to the increased rate of photoexcited charge carriers transferring from QDs to SWCNTs.<sup>24</sup> Our results also show that the fluorescence lifetime of QDs is reduced across the entire complex (Figure 1e). An order of magnitude decrease in QD fluorescence lifetime (from  $\approx 19$  to  $\approx 2$  ns) is observed comparing carboxyl QDs prior to and after SWCNT conjugation (see Supporting Information). In some regions where both the fluorescence signal and topography are high, an intermediate lifetime of  $\approx 6$  ns is observed (e.g., circle A in Figure 1e). We propose that the observed 6 ns lifetime in the QD aggregation area is due to the average of conjugated QDs and clustered or unconjugated QDs, which may exist on top of the SWCNT-conjugated QDs. This decreased average fluorescence lifetime of the QDs after conjugating to SWCNTs supports the hypothesis<sup>24</sup> that the rate of nonradiative relaxation of photoexcited QDs can be significantly in-

creased when the QDs are conjugated to metallic or small band gap semiconducting SWCNTs.

To further assess if this increased nonradiative relaxation is the result of increased charge transfer upon nanotube conjugation and to correlate the SWCNT Raman shift to the QD fluorescence intensity, a series of experiments were carried out independently on a micro-Raman system. Note that these experiments were not performed on the same mesoscopic sample structure described above. When excited at 632.8 nm, outside of the absorption window of the QDs, the Raman spectra resemble a typical sample of HiPCO SWCNTs, with no fluorescence background arising from the conjugated QDs. On the other hand, when the complex was excited with 514.5 nm, within the QD absorption window, QD fluorescence emission and SWCNT Raman signal can be observed in the same spectrum. To further establish the link between photoexcited carrier transfer in QD and Raman spectral shifts observed in SWCNTs, the sample was subjected to prolonged exposure of 514.5 nm light to photobleach the QD. As the QDs photobleach with time, the number of photoexcited QD carriers interacting with the nearby SWCNTs is expected to decrease drastically. Additionally, a decrease in the QD–SWCNT interaction upon QD photobleaching is expected to change the phonon frequency in the Raman spectra.

Figure 4 shows the Raman spectra of the conjugated QD–SWCNT sample at time zero (dashed red trace) and after 2.5 h of light exposure (solid black trace). At time zero, peaks at 203, 243, 264, and 295  $\text{cm}^{-1}$  were observed in the lower frequency radial breathing mode (RBM) region. The transitions correspond to nanotubes with diameters of 1.2, 1.0, 0.9, and 0.8 nm, respectively, which is consistent with previously measured HiPCO SWCNTs.<sup>30</sup> The measured RBM frequencies suggest that both metallic and semiconduct-

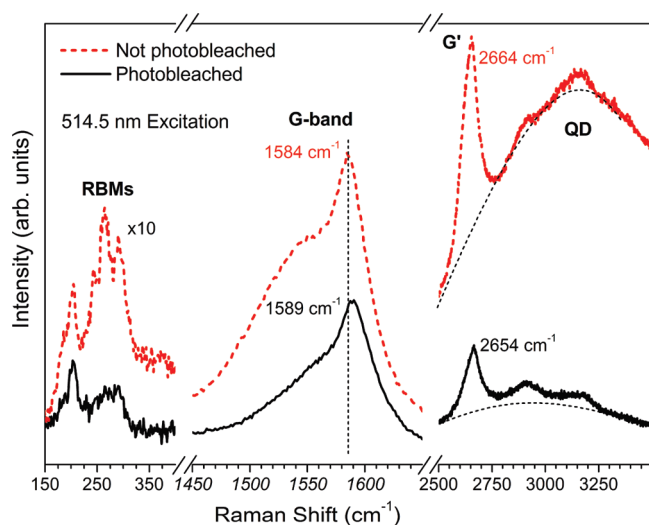


**Figure 4.** Raman spectra (514.5 nm excitation) of the conjugated QD–SWCNT sample at time zero (dashed red trace) and after 2.5 h of light exposure (solid black trace) to photobleach QDs in the sample. The dotted lines serve as guides to the eye.

ing SWCNTs are present in the sample. After 2.5 h of light exposure, the intensities of the 264 and 295  $\text{cm}^{-1}$  peaks were significantly reduced, suggesting that a fraction of the smaller diameter SWCNTs have been altered during the prolonged light exposure. Since bundled SWCNTs usually have fairly broad resonance windows, which can be shifted by the presence of QDs, it is not possible to identify the exact interband transition for the different nanotube species involved without using a large number of closely spaced laser excitation energies.

In the G band region around 1590  $\text{cm}^{-1}$ , the Raman spectrum of the conjugated sample can be clearly deconvolved into two components ( $G^-$  and  $G^+$ ), associated with A-symmetry TO and LO phonon modes in SWCNTs. Electron–phonon coupling predicts different G band features of metallic (M) and semiconducting (S) SWCNTs.<sup>31–33</sup> The asymmetric line shape of the  $G^-$  peak in our data suggests that some metallic nanotubes are being excited at the present excitation energy.

After the QDs were photobleached for 2.5 h with 514.5 nm laser light, a 5  $\text{cm}^{-1}$  shift was observed in the  $G^+$  band frequency of SWCNTs. Shifts in  $G^+$  band

frequency upon charge transfer have been observed previously in a number of doping and transport experiments combined with Raman measurements. In a simple model, the shift is introduced by changes in the C–C bond length in response to the injection of excess charge carriers from the nearby quantum dots in photoinduced charge separation events.<sup>34,35</sup> Figure 4 shows the region between 2400 and 4000  $\text{cm}^{-1}$ , which corresponds to the wavelength range between 587 and 648 nm. In addition to the Raman  $G'$  feature arising from the nanotubes, the large fluorescence background from the QD is observed. After the conjugated QDs undergo photoinduced oxidation from extended light exposure, the QD fluorescence blue-shifted while the fluorescence intensity decreased significantly.

## CONCLUSIONS

A hyperspectral imaging platform achieved by a smart integration of atomic force microscopy, its 2D autocorrelation analysis, and polarized hyperspectral imaging of QD–SWCNT heterostructures is presented. This integrated measurement provides rich information to effectively correlate the structural details of the constituent building blocks, QDs and SWCNTs, and their optoelectronic characteristics reflecting possible charge interactions. From polarized hyperspectral imaging results, when excited at energy above the absorption window of the QDs, the Raman spectrum of SWCNTs and the fluorescence spectrum QDs are achieved simultaneously. This capability opens a new possibility to probe photoinduced charge transfer from QDs to SWCNTs, bridging the properties observed in bulk and single nanotube studies. The QDs in the heterostructure exhibit significantly shortened fluorescence lifetime, indicating energy transfer by nonradiative coupling. More precise analysis of the heterostructure sample using micro-Raman spectroscopy provides a significant shift in the  $G^+$  Raman peak of the SWCNTs, and this shift correlates well with the fluorescence intensity associated with the QDs as they photobleach with time, implying photoinduced charge transfer from QDs to SWCNTs.

## METHODS

**Hybrid Sample Preparation.** The hybridization process is described in detail elsewhere.<sup>23</sup> SWCNTs were wrapped with 30-mer 5'-GT(GT)<sub>13</sub>GT-3' single-stranded DNA. CdSe/ZnS carboxyl-grouped QDs (NN-Laboratories) with an emission peak at around 602 nm were conjugated to the SWCNT by peptide bonding between the wrapping DNA and QDs. Specifically, the QD carboxyl groups are reacted with amine groups at the 3' end of DNA molecules attached to SWCNTs. The conjugation process was evaluated by optical spectroscopy techniques including FTIR and UV–vis measurements.<sup>23</sup> For AFM and confocal hyperspec-

tral imaging, 10  $\mu\text{L}$  of the sample solution was spin-cast on a hydrophilic glass substrate, followed by several washes using ultrapure water.

**Polarization-Dependent Hyperspectral Imaging.** For hyperspectral imaging of the QD–SWCNT complexes, we combined a CCD spectrometer (Princeton Instruments, Inc.) to a confocal microscope (Axiovert 135 TV, Zeiss) with a 100 $\times$  oil immersion objective lens (NA 1.45). A sample holder was fixed to a piezostage (LP 100, Mad City Laboratories, Inc., Madison, WI) controlled with LabVIEW software. The image was created by scanning a 10  $\mu\text{m}$   $\times$  10  $\mu\text{m}$  area. Each pixel was exposed for 2 s under a confocal spot of a *p*-polarized 488 nm exciting laser spot (Sapphire 488-20

CDRH, Coherent Co.) to obtain the emission spectrum. The hyperspectral image was constructed from  $128 \times 128$  photoluminescence spectra for the entire area of the sample. The raster scan and spectrum acquisition were synchronized with LabVIEW software operated in an external pulse mode. The polarization angle of the excitation laser spot was determined by measuring the transmission intensity through an analyzing polarizer in front of a photodiode detector. For polarization-dependent spectroscopic imaging, the sample was rotated by  $90^\circ$  for the second hyperspectral image. Detailed polarization-dependent 2D fluorescence and Raman intensity maps were generated from these images by integrating signal intensities within corresponding bandwidth regions.

**Fluorescence Lifetime Imaging.** We combined a lifetime measurement system (SPC830, Becker & Hickl GmbH) with the confocal microscopy system to confirm the energy transfer between QDs and SWCNTs. To do this, a Ti:sapphire laser system (Coherent Inc., Mira-900, pumped by Verdi-10 Nd:YVO<sub>4</sub> solid state laser) generated a beam with a 200 fs pulse width and 76 MHz repetition rate at a center wavelength of 922 nm. An SHG module (5-050, InRad) converted the laser wavelength to 461 nm. After a pulse picker (NEOS Technology) reduced the repetition rate to 7.6 MHz, the beam was delivered to the microscope via optical fiber. In the Scan-Sync-In mode, a lifetime map was created by raster-scanning a  $10 \mu\text{m} \times 10 \mu\text{m}$  area using a piezoelectric stage at a resolution of  $128 \times 128$  pixels by time-correlated single photon counting (TCSPC) board (Model SPC830, Becker and Hickl GmbH). The fluorescence lifetime curves were fitted by the single-exponential least  $\chi^2$  fitting algorithm in the SPCImage software (Becker & Hickl).

**Atomic Force Microscopy and 2D Autocorrelation Image Processing.** AFM images were taken with an Asylum Research MFP-3D in tapping mode using a silicon cantilever with an electron beam deposited carbon tip (Mikromasch). The best images were obtained with set points below 50% of the free tapping amplitude. Images have been flattened and plane-fit so that the substrate is at a uniform height, and the images were rotated for ease of display. Then 2D autocorrelation analysis to measure the alignment of SWCNTs was performed in MATLAB. In this method,  $16 \times 16$  pixel regions from the  $512 \times 512$  pixel AFM image were sequentially examined. The goal is to determine the local orientation of the SWCNTs within this small region. First, the autocorrelation (AC) image of this region image (RI) was calculated by

$$\text{AC} = \text{Real}[\text{FFT}^{-1}|\text{FFT}(\text{RI})|] \quad (1)$$

where FFT is the 2D fast Fourier transform function. Essentially, eq 1 is a method of comparing an image with itself under conditions of different offsets (*i.e.*, where one image is shifted in the  $x$  and/or  $y$  directions), and is done quickly in the frequency domain. When no offset is used, the correlation is maximized (see the center bright spot in the inset autocorrelation examples of Figure 2a). When the offset occurs along the same direction as a pattern in the image, the correlation will remain high (bright). If no pattern exists, the correlation will vanish.

When a pattern exists in the region image, it will also be observed in the autocorrelation image. For this study, we are particularly interested in the mean orientation of the texture of the phase image. First we examine summed intensity for different possible angles across the autocorrelation image. The angle which gives the maximum total intensity in the autocorrelation image corresponds to the orientation of the SWCNT bundles within this small region image. We will refer to this angle as the autocorrelation angle. The insets in Figure 2a show the autocorrelation images from two regions. Note that there is a pattern in the autocorrelation image from the region of bundled SWCNTs (lower right), while the autocorrelation image from the area between the bundles shows little discernible pattern. A line showing the autocorrelation angle (direction of brightest pattern) is displayed on each example. The length scale of this autocorrelation pattern provides information about how well-aligned the nanotubes are in this area. We fit the change in intensity of the autocorrelation along the autocorrelation angle as a function of distance from the origin to an exponential decay. The decay constant,  $\varepsilon$ , is related to the strength of the autocorrelation. The

angle of the red lines in the autocorrelation image (Figure 2a) represents the maximum angle of the local autocorrelation. The vector length of the lines corresponds to  $\varepsilon^{-1}$ . Therefore, longer lines, corresponding to smaller values of  $\varepsilon$ , represent areas with higher net orientation of the SWCNT bundles. To increase the number of data points for later calculations and to check the reproducibility of this technique, the autocorrelation analysis was repeated, offsetting each of the region images by 8 pixels in the  $x$ ,  $y$ , or  $x$  and  $y$  directions. Visual inspection of the alignment of the SWCNTs in the AFM phase image is in agreement with the 2D autocorrelation results. Estimated polarized Raman images were produced as described in the text by calculating the local average Raman intensity from autocorrelation regions where the autocorrelation decay constant  $\varepsilon \leq 2.5$  (to eliminate areas with weak autocorrelation), with  $\theta$  parallel (Figure 2b) and perpendicular (Figure 2c) to the long axis of the QD–SWCNT complex.

**Raman Spectroscopy.** The more detailed Raman experiments were carried out on a micro-Raman system (RM 1000, Renishaw), equipped with holographic diffraction gratings. The samples were spin-coated onto a glass coverslip and excited using an Ar<sup>+</sup> ion laser (514.5 nm) and a HeNe laser (632.8 nm). The Raman signal was collected through a microscope objective (50 $\times$ , 0.75 NA, Leica) via backscattering geometry. The laser excitation power was kept under 0.3 mW at all times.

**Acknowledgment.** We gratefully acknowledge H. Farhat and Ge. G. Samsonidze for informative discussions on the Kohn anomaly. We also gratefully acknowledge J.A. Fagan for providing DNA-wrapped SWCNTs. The work is partially supported by the National Research Council Fellowships (S.G.C. and M.L.C.). Certain equipment or materials are identified in this paper in order to specify the experimental procedure adequately. Such identification is not intended to imply endorsement by the National Institute of Standards and Technology, nor is it intended to imply that the materials or equipment identified are necessarily the best available.

**Supporting Information Available:** Additional AFM images of the heterostructures, fluorescence lifetime data of QDs before and after SWCNT conjugation, and a video of the hyperspectral image. This material is available free of charge via the Internet at <http://pubs.acs.org>.

## REFERENCES AND NOTES

- Soman, C. P.; Giorgio, T. D. Quantum Dot Self-Assembly for Protein Detection with Sub-picomolar Sensitivity. *Langmuir* **2008**, *24*, 4399–4404.
- Haremza, J. M.; Hahn, M. A.; Krauss, T. D. Attachment of Single CdSe Nanocrystals to Individual Single-Walled Carbon Nanotubes. *Nano Lett.* **2002**, *2*, 1253–1258.
- Zheng, M.; Jagota, A.; Strano, M. S.; Santos, A. P.; Barone, P.; Chou, S. G.; Diner, B. A.; Dresselhaus, M. S.; McLean, R. S.; Onoa, G. B.; Samsonidze, G. G.; Semke, E. D.; Usrey, M.; Walls, D. J. Structure-Based Carbon Nanotube Sorting by Sequence-Dependent DNA Assembly. *Science* **2003**, *302*, 1545–1548.
- Snee, P. T.; Somers, R. C.; Nair, G.; Zimmer, J. P.; Bawendi, M. G.; Nocera, D. G. A Ratiometric CdSe/ZnS Nanocrystal pH Sensor. *J. Am. Chem. Soc.* **2006**, *128*, 13320–13321.
- Mirkin, C. A.; Letsinger, R. L.; Mucic, R. C.; Storhoff, J. J. A DNA-Based Method for Rationally Assembling Nanoparticles into Macroscopic Materials. *Nature* **1996**, *382*, 607–609.
- Cha, J. N.; Bartl, M. H.; Wong, M. S.; Popitsch, A.; Deming, T. J.; Stucky, G. D. Microcavity Lasing from Block Peptide Hierarchically Assembled Quantum Dot Spherical Resonators. *Nano Lett.* **2003**, *3*, 907–911.
- Li, F.; Zhang, Z. P.; Peng, J.; Cui, Z. Q.; Pang, D. W.; Li, K.; Wei, H. P.; Zhou, Y. F.; Wen, J. K.; Zhang, X. E. Imaging Viral Behavior in Mammalian Cells with Self-Assembled Capsid-Quantum-Dot Hybrid Particles. *Small* **2009**, *5*, 718–726.
- Peng, X. H.; Chen, J. Y.; Misewich, J. A.; Wong, S. S. Carbon Nanotube–Nanocrystal Heterostructures. *Chem. Soc. Rev.* **2009**, *38*, 1076–1098.

9. Deshpande, A.; Shah, P.; Gholap, R. S.; Gupta, N. M. Interfacial and Physico-Chemical Properties of Polymer-Supported CdS Center Dot ZnS Nanocomposites and Their Role in the Visible-Light Mediated Photocatalytic Splitting of Water. *J. Colloid Interface Sci.* **2009**, *333*, 263–268.
10. Ahmad, A.; Kern, K.; Balasubramanian, K. Selective Enhancement of Carbon Nanotube Photoluminescence by Resonant Energy Transfer. *ChemPhysChem* **2009**, *10*, 905–909.
11. Skrabalak, S. E.; Xia, Y. A. Pushing Nanocrystal Synthesis toward Nanomanufacturing. *ACS Nano* **2009**, *3*, 10–15.
12. Landi, B. J.; Castro, S. L.; Ruf, H. J.; Evans, C. M.; Bailey, S. G.; Raffaele, R. P. CdSe Quantum Dot—Single Wall Carbon Nanotube Complexes for Polymeric Solar Cells. *Sol. Energy Mater. Sol. Cells* **2005**, *87*, 733–746.
13. Ravindran, S.; Chaudhary, S.; Colburn, B.; Ozkan, M.; Ozkan, C. S. Covalent Coupling of Quantum Dots to Multiwalled Carbon Nanotubes for Electronic Device Applications. *Nano Lett.* **2003**, *3*, 447–453.
14. Ravindran, S.; Bozhilov, K. N.; Ozkan, C. S. Self Assembly of Ordered Artificial Solids of Semiconducting ZnS Capped CdSe Nanoparticles at Carbon Nanotube Ends. *Carbon* **2004**, *42*, 1537–1542.
15. Tsuya, D.; Suzuki, M.; Aoyagi, Y.; Ishibashi, K. Quantum Dots and Their Tunnel Barrier in Semiconducting Single-Wall Carbon Nanotubes with a p-Type Behavior. *Jpn. J. Appl. Phys.* **2005**, *44*, 2596–2599.
16. Landi, B. J. Quantum Dot-Single Wall Carbon Nanotube Complexes for Tunable Optoelectronic Microsystems Sensors. Ph.D. Thesis, Rochester Institute of Technology, 2006.
17. Li, F. S.; Son, D. I.; Kim, T. W.; Ryu, E.; Kim, S. Carrier Transport Mechanisms of Bistable Memory Devices Fabricated Utilizing Core—Shell CdSe/ZnSe Quantum-Dot/Multi-Walled Carbon Nanotube Hybrid Nanocomposites. *Nanotechnology* **2009**, *20*, 085202.
18. Li, F. S.; Cho, S. H.; Son, D. I.; Kim, T. W.; Lee, S. K.; Cho, Y. H.; Jin, S. H. UV Photovoltaic Cells Based on Conjugated ZnO Quantum Dot/Multiwalled Carbon Nanotube Heterostructures. *Appl. Phys. Lett.* **2009**, *94*, 111906.
19. Li, F.; Son, D. I.; Cho, S. H.; Kim, W. T.; Kim, T. W. Flexible Photovoltaic Cells Fabricated Utilizing ZnO Quantum Dot/Carbon Nanotube Heterojunctions. *Nanotechnology* **2009**, *20*, 155202.
20. Li, F.; Son, D. I.; Cho, S. H.; Kim, T. W. Electrical Bistabilities and Operating Mechanisms of Memory Devices Fabricated Utilizing ZnO Quantum Dot—Multi-Walled Carbon Nanotube Nanocomposites. *Nanotechnology* **2009**, *20*, 185202.
21. Kongkanand, A.; Tvrđy, K.; Takechi, K.; Kuno, M.; Kamat, P. V. Quantum Dot Solar Cells. Tuning Photoresponse through Size and Shape Control of CdSe-TiO<sub>2</sub> Architecture. *J. Am. Chem. Soc.* **2008**, *130*, 4007–4015.
22. Li, X. L.; Zhang, L.; Wang, X. R.; Shimoyama, I.; Sun, X. M.; Seo, W. S.; Dai, H. J. Langmuir—Blodgett Assembly of Densely Aligned Single-Walled Carbon Nanotubes from Bulk Materials. *J. Am. Chem. Soc.* **2007**, *129*, 4890–4891.
23. Zhou, Z.; Kang, H.; Clarke, M. L.; Silvia, H.; De, P. L.; Zhao, M.; Fagan, J. A.; Shapiro, A.; Nguyen, T.; Hwang, J. Water Soluble DNA-Wrapped Single-Wall Carbon Nanotube/Quantum Dot Complexes. *Small* **2009**, *5*, 2149–2155.
24. Biju, V.; Itoh, T.; Baba, Y.; Ishikawa, M. Quenching of Photoluminescence in Conjugates of Quantum Dots and Single-Walled Carbon Nanotube. *J. Phys. Chem. B* **2006**, *110*, 26068–26074.
25. Hwang, J.; Gheber, L. A.; Margolis, L.; Edidin, M. Domains in Cell Plasma Membranes Investigated by Near-Field Scanning Optical Microscopy. *Biophys. J.* **1998**, *74*, 2184–2190.
26. Duesberg, G. S.; Loa, I.; Burghard, M.; Syassen, K.; Roth, S. Polarized Raman Spectroscopy on Isolated Single-Wall Carbon Nanotubes. *Phys. Rev. Lett.* **2000**, *85*, 5436–5439.
27. Fagan, J. A.; Simpson, J. R.; Landi, B. J.; Richter, L. J.; Mandelbaum, I.; Bajpai, V.; Ho, D. L.; Raffaele, R.; Walker, A. R. H.; Bauer, B. J.; Hobbie, E. K. Dielectric Response of Aligned Semiconducting Single-Wall Nanotubes. *Phys. Rev. Lett.* **2007**, *98*, 147402.
28. Gommans, H. H.; Alldredge, J. W.; Tashiro, H.; Park, J.; Magnuson, J.; Rinzler, A. G. Fibers of Aligned Single-Walled Carbon Nanotubes: Polarized Raman Spectroscopy. *J. Appl. Phys.* **2000**, *88*, 2509–2514.
29. Islam, M. F.; Milkie, D. E.; Kane, C. L.; Yodh, A. G.; Kikkawa, J. M. Direct Measurement of the Polarized Optical Absorption Cross Section of Single-Wall Carbon Nanotubes. *Phys. Rev. Lett.* **2004**, *93*, 037404.
30. Kukovec, A.; Kramberger, C.; Georgakilas, V.; Prato, M.; Kuzmany, H. A. Detailed Raman Study on Thin Single-Wall Carbon Nanotubes Prepared by the HiPCO Process. *Eur. Phys. J. B* **2002**, *28*, 223–230.
31. Piscanec, S.; Lazzeri, M.; Robertson, J.; Ferrari, A. C.; Mauri, F. Optical Phonons in Carbon Nanotubes: Kohn Anomalies, Peierls Distortions, and Dynamic Effects. *Phys. Rev. B* **2007**, *75*, 035427.
32. Samsonidze, G. G.; Barros, E. B.; Saito, R.; Jiang, J.; Dresselhaus, G.; Dresselhaus, M. S. Electron-Phonon Coupling Mechanism in Two-Dimensional Graphite and Single-Wall Carbon Nanotubes. *Phys. Rev. B* **2007**, *75*, 155420.
33. Di Donato, E.; Tommasini, M.; Castiglioni, C.; Zerbi, G. Assignment of the G(+) and G(−) Raman Bands of Metallic and Semiconducting Carbon Nanotubes Based on a Common Valence Force Field. *Phys. Rev. B* **2006**, *74*, 184306.
34. Rao, A. M.; Eklund, P. C.; Bandow, S.; Thess, A.; Smalley, R. E. Evidence for Charge Transfer in Doped Carbon Nanotube Bundles from Raman Scattering. *Nature* **1997**, *388*, 257–259.
35. Debarre, A.; Jaffiol, R.; Julien, C.; Nutarelli, D.; Richard, A.; Tchenio, P. Specific Raman Signatures of a Dimetallofullerene Peapod. *Phys. Rev. Lett.* **2003**, *91*, 085501.